Real-time in situ optical tracking of oxygen vacancy migration in memristors

Giuliana Di Martino [1,2,5 ✉], Angela Demetriadou[3,5], Weiwei Li[2,5], Dean Kos [1], Bonan Zhu[2], Xuejing Wang[4], Bart de Nijs [1], Haiyan Wang [4], Judith MacManus-Driscoll [2] and Jeremy J. Baumberg[1 ✉]

Resistive switches, which are also known as memristors, are low-power, nanosecond-response devices that are used in a range of memory-centric technologies. Driven by an externally applied potential, the switching mechanism of valence change resistive memories involves the migration, accumulation and rearrangement of oxygen vacancies within a dielectric medium, leading to a change in electrical conductivity. The ability to look inside these devices and understand how morphological changes characterize their function has been vital in their development. However, current technologies are often destructive and invasive. Here, we report a non-destructive optical spectroscopy technique that can detect the motion of a few hundred oxygen vacancies with nanometre-scale sensitivity. Resistive switches are arranged in a nanoparticle-on-mirror geometry to exploit the high optical sensitivity to morphological changes occurring in tightly confined plasmonic hotspots within the switching material. Using this approach, we find that nanoscale oxygen bubbles form at the surface of a strontium titanate memristor film, leading ultimately to device breakdown on cycling.

Resistive random access memories (RRAMs) are promising emerging devices for logic-in-memory operations due to their high-density integration and scalability, ultra-fast access times, low power consumption and ease of fabrication[1]. RRAMs can be classified as conductive bridge random access memories (CBRAMs, also called electrochemical metallization cells) or redox random access memories (ReRAMs, also called valence change mechanism cells)[2,3]. In CBRAM cells, a nanoscale conductive metallic path between a working electrode/anode (often electrochemically active, such as silver or copper) and a counter-electrode/cathode (often inert, such as platinum, gold or titanium nitride) is formed or broken by the generation, movement and reduction of mobile metal cations (that is Ag^+ or Cu^{2+}, for example)[4]. ReRAMs occur in a wide range of transition metal oxides[5,6] and are typically triggered by migration of anions such as oxygen (usually described by the motion of the corresponding oxygen vacancies). The subsequent modified stoichiometry leads to redox reactions from valence changes of the cation sublattice and changes in the electronic conductivity at the electrode interface[7–10]. Sometimes, ions can oxidize upon reaching the positive electrode via the half-reaction $2O^{2-} \rightarrow 4e^- + O_{2(g)}$, forming bubbles of oxygen gas[11]. With such ReRAM devices, it is important to identify and understand the failure mechanisms that impact endurance and variations in memristive device parameters, thus avoiding the extra energy required to eliminate the impact of process variations, which modify geometries, thicknesses and contact areas[6,12,13].

Widely used characterization methods—such as voltage-sweep and voltage-pulse measurements, electrochemical cyclic voltammetry, and ex situ and in situ electron microscopy—do not provide a full description of the switching dynamics in either CBRAM or ReRAM. Slow device switching in voltage-sweep measurements

leads to artefacts in the switching behaviour[14]. Pulse measurements do not characterize the full voltage–current behaviour of the device[15,16], whereas cyclic voltammetry does not distinguish the very localized resistive switching effects, with little insight into the morphology and geometry of the formed filaments[17]. Ex situ transmission electron microscopy (TEM) allows for high-resolution imaging of filaments and metal clusters as well as the modified morphology of the switching material, but only before and after switching[18–20].

In ReRAM, the use of TEM can be challenging due to the low image contrast between oxygen-rich and -deficient regions. Nevertheless, some studies have imaged conductive phases in ReRAM cells. The formation and rupture of a sub-stoichiometric and conductive Magnéli phase in TiO_2 with a diameter as low as 10 nm has, for example, been demonstrated[7]. Additionally, in situ TEM operation conditions and samples differ from resistive switches in practical applications. Devices are typically prepared on electron-transparent silicon nitride windows and the electrons used for imaging can perturb the drift of the charged ions.

Large optical field enhancements in nanoplasmonic systems have proven useful in understanding the dynamics involved in the switching processes in CBRAM devices[21–23]. New information can be obtained without perturbing the system by creating optically accessible CBRAM switches and monitoring in real time the scattering signal coming from the plasmonic field tightly confined to the nanometre-scale switching gap. The optical spectrum of the plasmonic hotspot in the junction shows the creation and destruction of conductive channels between the electrodes, tracking morphological changes occurring in the switching material. In this Article, we adopt this technique to observe the valence change mechanism in ReRAM devices. In particular, we examine the motion of oxygen vacancies within the switching
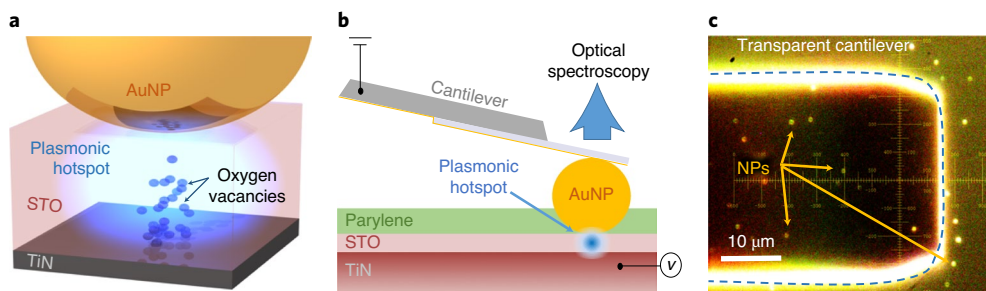
Fig. 1 | Memristive device in a plasmonic geometry. a, ReRAM in an NPoM geometry, with plasmonic field tightly confined in the spacer material, STO, between an AuNP and the TiN film. **b**, Optical spectroscopy is performed through a transparent but electrically conductive cantilever that is used to contact each individual AuNP isolated by the surrounding insulating parylene layer. **c**, Dark-field top view of AuNPs on an STO layer, seen through the cantilever.

material strontium titanate ($SrTiO_3$), which is otherwise invisible to non-invasive electron microscopy techniques.

Device structure and experimental set-up

We fabricated cells with a conventional TiN/$SrTiO_3$ (TiN/STO) layer stack and a gold-nanoparticle (AuNP) top electrode (Fig. 1a,b). The STO acts as switching material, while the bottom conducting TiN layer forms the counter-electrode. Being widely adopted for ReRAM cells[24–26], STO is an ideal model material system. We emphasize that the optical properties of TiN follow a Drude-like behaviour, similar to Au, thus forming nanogaps with strong plasmonic field confinement when close to metallic nanoparticles (nanoparticle-on-mirror (NPoM) geometry[27]; Fig. 1a).

The NPoMs were individually electrically contacted from the top using a flexible transparent Si_3N_4 tip-less cantilever coated with 3-nm Cr and 6-nm Au, yielding a resistance of ~$3\,\Omega\,\square^{-1}$ (Fig. 1b). This allowed unobstructed observation of AuNP scattering under the cantilever through dark-field spectroscopy (Fig. 1b,c). The density of AuNPs (80-nm diameter) on the sample surface was further reduced in the deposition phase to ensure that the NPoM structures were individually contacted, with the large cantilever area ensuring edge scattering was not collected. Compared to the highly scattering atomic force microscopy (AFM) tips, this cantilever contacting allows optical access to the very inner regions of the device. To further ensure electrical connection only through the AuNP without any direct cantilever contact with the STO surface, the system was conformally coated with an insulating parylene layer, which was dry-etched to expose the AuNP crown while maintaining a pinhole-free insulating barrier over the surrounding surface (Methods).

The valence change mechanism is responsible for the switching process in this cell, with the oxygen vacancies experiencing drift under bias through the STO layer. Resistive switching is enabled by a voltage (typically 8 V–12 V) applied to the TiN. We used <10 µA current compliance to restrict the maximum current in the low-resistive on state (LRS).

In our measurements, the cantilever was gradually lowered into contact with the top of an isolated NPoM structure until it was locally parallel to the device top surface. The cantilever position and tilt orientation were controlled within <1 nm and <0.2°, respectively, using a piezoelectric stage while observing the wedged interference fringes created by the cantilever when approaching the Au mirror. Compared to the >10 GPa van der Waals forces across these nanometre-scale metal gaps, the cantilever makes little difference (~0.04 GPa) because it accommodates contact by bending along its 200 µm length (Methods). The pressures used here are within a safe range where they play no role in the switching (Supplementary Section G)[28].

We recorded the dark-field scattering spectra and voltage–current signals simultaneously. The localized plasmons of each AuNP couple to their image charges in the TiN film underneath the STO spacer layer, forming a confined plasmonic hotspot, similar to a nanoparticle dimer[29,30]. The NPoM configuration has been investigated extensively[27]. The optical response of this system was measured by illuminating the sample with a white-light beam incident at 60° and collecting the scattered light through a dark-field objective (Methods). Light was collected by a cooled spectrometer and a charge-coupled device (CCD) camera.

Experimental optical investigation of switching cycles

We focused our attention on two sets of samples with STO thicknesses of $d = 8$ nm (D_8, Fig. 2a–c) and 4 nm (D_4, Fig. 2d–i), respectively, as demonstrated via cross-sectional TEM (Supplementary Fig. 4). The results are representative, but the behaviour for each specific cell differs slightly in the details—spectral changes are consistently observed only upon switching, but the change in intensity or peak position can vary due to the nature of the switching mechanism (Supplementary Fig. 1), which involves stochastic processes and a complex interplay between electrochemical and diffusion effects (Supplementary Section H). The cells here switch to the LRS at a set voltage V_{SET} defined as the voltage where the current abruptly changes from <40 pA to several nanoamperes (Fig. 2b) or microamperes (Fig. 2f). Applying a negative voltage results in a reset of the cell (switching back to the high-resistance off state, HRS).

For the D_8 sample, the AuNP scattering spectra show a strong plasmon resonance at $\lambda_1 \approx 610$ nm (Fig. 2a,c(I)). Focusing on times preceding the clear electrical switching event ($20\,s < t < 30\,s$), the longer-wavelength peak $\lambda_2 \approx 780$ nm grows (Fig. 2a,c(II)). After the set event at ~30 s, the total conductance reaches $10^{-5}G_0$ ($30\,s < t < 70\,s$), well below that for an atomic point contact ($G_0 = 77.5\,\mu S$ is the quantum conductance), as expected for ReRAM systems with narrow conductive filaments[31]. In fact, the presence of oxygen vacancy paths in the dielectric gives extended bands in the gap[32], resulting in conductance $G \approx G_0$ for one vacancy path[33] and $G \ll G_0$ when several vacancies are removed from the single-vacancy filament, hence positioning the energy of the first subband just above the electrode Fermi level[31]. Although for this device the peak scattering λ_1 changes little with time, its intensity transiently halves following the switching event (Fig. 2a,c(III)). By contrast, the longer-wavelength peak λ_2 retains its intensity with a redshift of only a few nanometres. After the reset event ($t > 70\,s$), the λ_1 peak intensity increases to its value before switching, while the λ_2 peak remains unchanged (Fig. 2a,c(IV)). This highlights the non-reversibility of the ReRAM switching process, which is unable[24] to bring the system back to the morphology of a pristine cell (I). Only three switching cycles are observed for the D_8 sample.
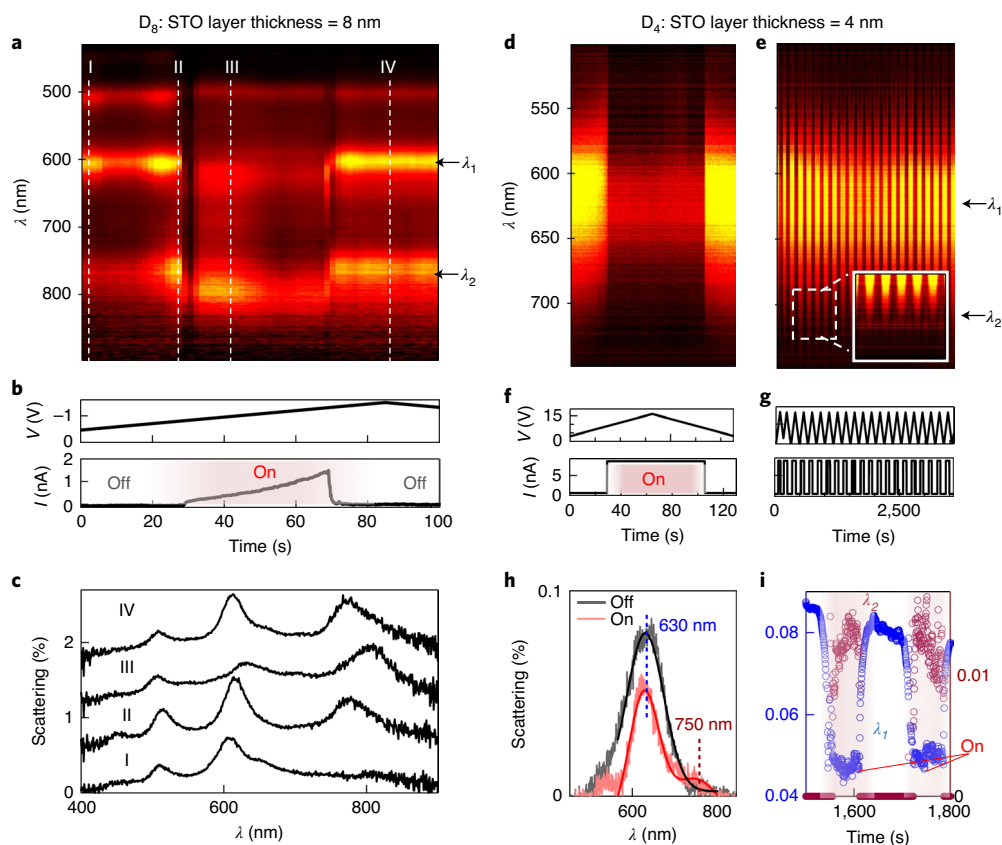
Fig. 2 | Switching cycles of the NPoM memristive cell. a,b, Scattering intensity (**a**) collected simultaneously with the electrical signal (voltage and current) (**b**) from a single AuNP on D_8. **c**, Spectra for a pristine sample (I), the device pre-switching (II), the device switched on (III) and at reset of the device into the off state (IV) at times corresponding to the dashed lines in **a**. A clear peak appears in the infrared ($\lambda_2 \approx 780–800$ nm) without disappearing upon reset. **d–g**, Scattering intensity of single (**d**) and multiple (**e**) switching cyles collected simultaneously with the electrical signal (voltage and current) (**f,g**) from a single AuNP on D_4. Weaker scattering is observed with a strong $\lambda_1 \approx 630$ m peak and a weak $\lambda_2 \approx 750$ nm peak (highlighted in the inset in **e**). **h**,Detailed on (red) and off (black) spectra with multi-peak fits. **i**, Extracted $\lambda_1 \approx 630$ nm (blue) and $\lambda_2 \approx 750$ nm (purple) intensity oscillations with switching (on, shaded).

Turning our attention to the D_4 sample (Fig. 2d–i), we observe switching over multiple cycles when the applied voltage is repeatedly switched (Fig. 2e,g). Again, a shorter-wavelength mode $\lambda_1 \approx 630$ nm is identified, with an intensity that reduces upon switching, as in the D_8 sample (Fig. 2d,h,i). A longer-wavelength peak $\lambda_2 \approx 750$ nm is again visible upon switching (Fig. 2h, red), but, in contrast with the D_8 sample, it is much weaker and completely disappears upon reset (Fig. 2i, purple). The D_4 sample thus shows fully reversible switching, highlighting how this system can return to the morphology of a pristine cell. Although switching events here progress over tens of seconds, faster voltage sweeps result in faster switching.

To confirm that the measured optical signatures arise from the bias-induced drift of oxygen vacancies within the STO layer, we studied samples where the oxygen vacancies had been substantially removed by annealing (cooled in 40-kPa O_2 after film growth). No switching events were measured and a completely constant scattering signal was observed, even when voltage was applied (Supplementary Fig. 2).

Tracking oxygen vacancies drift and nanobubbles formation

To link the optical signatures observed experimentally with the various morphology regimes, we used a combination of density functional theory (DFT) calculations and finite-difference time-domain (FDTD) simulations (Methods) to meticulously analyse how oxygen

vacancy drift influences the plasmonic modes in STO layers, and thus the experimentally measured spectra.

In the NPoM structure, aligning the lower nanoparticle facet (typically $w = 20–30$ nm wide) against the flat mirror (Fig. 3c,d) creates a thin plasmonic cavity that supports multiple 'cavity' resonances or gap modes[34]. Plasmon oscillations in the nanoparticle, perpendicular to the surface, induce image charges within the TiN mirror, confining the field within the gap and giving rise to the plasmon cavity modes studied extensively elsewhere[35–37]. The plasmon cavity modes appear at specific energies depending on the mirror (TiN) and nanoparticle (Au) materials as well as the presence of a TiO$_2$ layer (confirmed by TEM; Supplementary Fig. 4), resulting from oxidation of the top few nanometres of TiN during STO growth (Fig. 3c,d). Figure 3b shows the field enhancement in the middle of the STO layer, where the energetically lowest mode appearing at ~760–790 nm (depending on the STO thickness) is a dark mode, l_{11}. The first bright mode appears at ~680 nm for both devices; this is commonly referred to as the 'dipole' mode, or l_{10}. The quadrupole resonance l_{20} appears at ~550 nm for both devices. The scattering cross-sections and radiative spectra of the two devices are shown in Fig. 3e–h, where only the l_{10} mode radiates significantly, while the l_{11} mode absorbs, producing a dip in the radiative spectra. Hence, the scattering peak measured at longer wavelengths >800 nm is not in fact a resonance of the system, but is the result of the superposition of the dark mode l_{11} on the broad tail of the bright
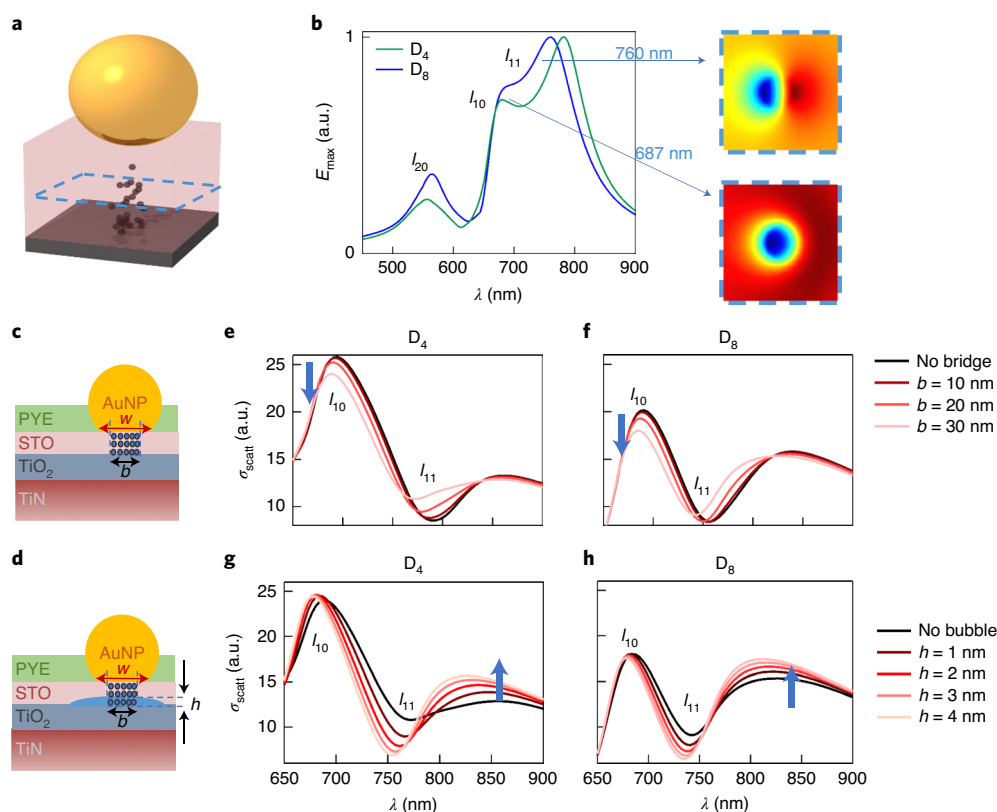
Fig. 3 | Numerical simulation of optical gap modes. a, Geometry of the nanoparticle above the oxygen vacancy accumulation region. Field cuts are taken over the mid-gap blue dashed plane parallel to the substrate. **b**, First-order bright and dark modes l_{10} and l_{11} at 687 nm and 760 nm and second-order mode l_{20} at 550 nm. **c,d**, NPoM with an oxygen-vacancy-rich bridge linking the AuNP (facet $w = 30$ nm) to the surface (**c**) and with O_2 bubble formation (**d**). **e–h**, Corresponding FDTD simulation modes for the two STO thicknesses D_4 (**e,g**) and D_8 (**f,h**) with varying bridge width $b = 0$, 10, 20 and 30 nm (**e,f**) and oxygen bubble height $h = 0$, 1, 2, 3 and 4 nm after a bridge of $b = 30$ nm is formed (**g,h**).

mode l_{10}. Our experiments show narrower resonances, probably due to weaker absorption in the measured system than expected from literature dielectric constants[38,39], but the resonances are fairly consistent between the experiment and simulation.

The oxygen vacancy bridge formed between the nanoparticle and the TiN mirror allows current to flow between the two structures when a bias is applied. The optical properties of the STO change when it fills with oxygen vacancies. To calculate this, we used DFT considering a $2 \times 2 \times 2$ supercell with 24 oxygens to simulate $SrTiO_{3-\delta}$. From the energy levels, we obtained the corresponding dielectric functions, with vacancy concentrations from $\alpha = 4$ to 20% (1/24 to 5/24 in the supercell) (Supplementary Fig. 5).

To parameterize the influence of oxygen-vacancy-rich bridges on the spectral far-field response of the NPoM system, we incorporated these DFT optical properties into FDTD simulations of the bridge between TiN and an 80-nm AuNP with fixed circular facet diameter $w = 30$ nm (Fig. 3c). This was progressively conductively connected to the Au surface through a bridge with a content of 4% oxygen vacancies in the centre of the AuNP facet. The diameter of the cylindrical conductive bridge was varied from $b = 0$ to 30 nm, from no connection to a bridge with a size that equals the full facet, giving the optical spectra shown in Fig. 3e,f. The l_{10} resonance blue-shifts and its scattering amplitude decreases by up to ~30% as the vacancy bridge is formed. This corresponds well with the experiment (Fig. 2a,d), where the scattering of both devices decreases at 600 nm when current flows between the AuNP and the TiN mirror (that is, the device was on), although the peak positions are slightly shifted. Although the behaviour is qualitatively predicted, the inten-

sity change (~150% for experiments in D_4; Supplementary Fig. 14) might be influenced by slight variations of refractive index from the DFT predictions.

By contrast, the peak at 840 nm is barely affected by the conductive vacancy bridge, indicating that an additional process, more dominant for D_8, occurs. To explain the observed spectral shifts we are forced to conclude that, with enough oxygen vacancies, the dense oxygen at the other electrode reversibly converts to O_2 gas, strongly perturbing the scattering response. As previously found, ultrathin oxide layers can reversibly form oxygen under high fields[40]. To study the influence of O_2 content on the spectral far-field response, FDTD simulations were performed with a fixed facet diameter of $w = 30$ nm, fixed bridge size of $b = 30$ nm and thin dome-shaped oxygen bubble height at the STO interface that varied from $h = 0$ nm to 4 nm (Fig. 3g,h). These scattering spectra show that the O_2 reservoir has a very strong impact on the scattering strength at ~840 nm, but negligible change to the l_{10} mode scattering peak at ~700 nm. Note that, for D_8, the scattering intensity at 840 nm is substantially brighter for larger O_2 reservoirs and reaches similar values to the l_{10} mode scattering at ~700 nm. This behaviour is in agreement with the experimental results of Fig. 2a–c, where the $\lambda_2 \approx 800$ nm peak has stronger scattering intensity.

From our simulations, we thus conclude that changes to the main bright l_{10} mode at $\lambda_1 \approx 600$ nm are due to the formation of the current-carrying vacancy bridge, which eventually turns the device on, while changes to the $\lambda_2 \approx 800$ nm peak come from superposed l_{10} and l_{11} modes arising from formation of an O_2 nanoreservoir at the STO/TiO_2 interface[41]. Each spectral peak
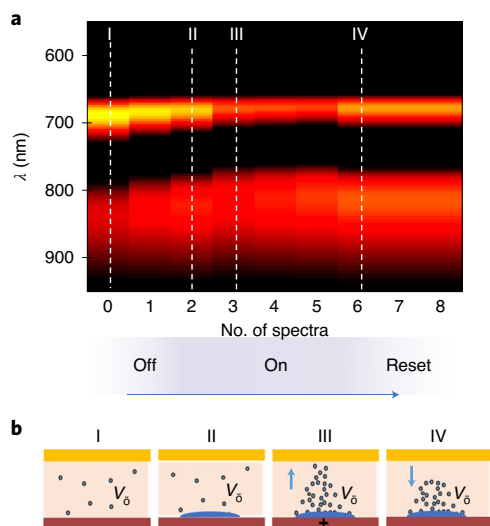
Fig. 4 | Numerical simulations of optical modes through the first switching cycle. a,b, Scattering intensities (**a**) of the structures in **b**: oxygen vacancies distributed through pristine sample (I), device pre-switching with $h = 2\,nm$ (II), device switched on with $h = 2\,nm$ and $b = 30\,nm$ (III) and resetting of the device into the off state with $h = 4\,nm$ (IV).

can be independently used as a signature for real-time and in situ readout of morphological changes occurring in the STO switching material, with few-nanometre resolution (lateral optical-mode full-width at half-maximum $\sqrt{wd} \approx 11\,nm$ and $15\,nm$ for D_4 and D_8, respectively; Supplementary Fig. 12). Changes in l_{10} scattering intensity enable us to resolve the construction of these oxygen vacancy bridges for long times before the actual set event, even though the electrical signature only shows a sharp transition into the on state (Supplementary Fig. 14c). To highlight this ability to link nanoscale morphological changes to scattering spectra, we simulated the full evolution through a switching cycle (Fig. 4a). The pristine sample (no. 0), with no conductive bridge and no O_2 bubble, initially grows through (nos. 1–2) an O_2 reservoir of height $h = 2\,nm$ to a conductive bridge (on state, nos. 3–5) of $w = 30\,nm$ together with an O_2 reservoir of $h = 2$–$4\,nm$. Afterwards (reset, nos. 6–8), no conductive bridge remains, but an oxygen bubble of $h = 4\,nm$ is left behind. Although our model is necessarily simplistic, it is able to reproduce the experimental switching event depicted in Fig. 2a, with the corresponding spectra I, II, III and IV matching between experiment and simulations (Fig. 4), supporting our explanation. Comparing the intensity change for the λ_2 peak both in experimental and simulated scattering spectra enables us to optically track the bubble formation and its enlargement (Supplementary Fig. 13). The ~90% increase in scattering intensity at λ_2 in the pre-switching phase (II) of D_8 matches our FDTD simulations of the long-wavelength peak when an 8-nm O_2 bubble is formed in the STO layer. This highlights the substantial material transformation that characterizes the poor switching behaviour of D_8.

The first switching event of D_8 demonstrates non-reversible behaviour and shows the considerable stress built into the STO. This results in non-stable devices unable to perform multiple cycles, so that early breakage is observed. By contrast, D_4 (Fig. 2d–g) is characterized by continuous repeatable switching. From its spectroscopic signature, showing the plasmonic modes λ_1 consistently decreasing (oxygen vacancy accumulation) and λ_2 increasing (O_2 bubble formation) in intensity with switching over multiple cycles, we conclude that the O_2 reservoir is fully reabsorbed into the structure after every reset event. In our study, the devices with 8-nm STO thickness

were more prone to fail than devices with 4-nm STO thickness, which could undergo hundreds of cycles (Supplementary Fig. 15d). The optical signatures of oxygen bubbles present in the 8-nm device (which possibly has a larger (thicker) STO reservoir of vacancies) suggest this plays a significant role in the failure mechanism.

Similar results were obtained for other devices, showing how spectroscopy is able to characterize the movement of oxygen vacancies before any electrical transport changes can be resolved (Supplementary Fig. 14c), as well as showing that oxygen nano-bubble formation at the TiN/STO interface is a key cause of failure. We underline how such optical spectroscopy finally enables an improved understanding of the causes leading to device breakdown. This is achieved with an in situ technique that tracks, in real time, under ambient conditions and without perturbing the system, oxygen vacancy migration within a few nanometres of the switching layer, which can thus be combined with other techniques and environmental conditions.

Conclusions

We have linked the fields of nanoscale device engineering and plasmon-enhanced light–matter interactions to implement optically accessible resistive switches. A conductive transparent cantilever with nanoparticle-mediated electrical contacts provides a useful and non-destructive method to characterize the resistive switching effect in ReRAM devices. Avoiding the impact of electron beams and the need for lateral junctions (required for electron beams to access the region of the filament formation) are key benefits of this approach. Our experimental and numerical investigation generates new insight into the mechanism behind drift and accumulation of oxygen vacancies, the creation of a conductive channel between the electrodes, and formation of nanometre-size oxygen bubbles at the lower switching material interface. Our numerical framework couples each spectral peak to the drift of oxygen vacancies and to the formation of an O_2 reservoir at the STO/TiO$_2$ interface. The change of scattering intensity of the optical mode assigned to the bridge formation enables us to resolve the drift of oxygen vacancies in the ~30 s before the set event, showing only a sharp transition when the on state is reached. Our approach also helps to identify the breakdown mechanisms upon cycling. Future improvements in the technique will aim to decrease the switching voltages by reducing the dielectric spacer thickness, which has the additional benefit of trapping the light more tightly in the nanogap, thus increasing the spectroscopic signatures of filament dynamics and accessing faster timescales.

Methods

Sample preparation. Epitaxial SrTiO$_3$/TiN bilayer films were grown on (001)-oriented MgO substrates by pulsed laser deposition (PLD). Before growing the bilayer films, (001)-oriented MgO substrates were annealed in situ at 950 °C for 2 h in vacuum. The TiN layer (~40 nm) was fabricated using a substrate temperature of 650 °C in an argon partial pressure of 1 mtorr with a laser fluence of 1.5 J cm^{-2}. The substrate temperature was then increased to 750 °C in an oxygen partial pressure of 1 mtorr for growing the SrTiO$_3$ layer. After deposition, the films were cooled to room temperature at a rate of 10 °C min^{-1} under an oxygen pressure of 1 mtorr. To further remove oxygen vacancies, some films were cooled under an oxygen partial pressures of 300 torr. The growth dynamics were investigated by real-time monitoring of the intensity variations of various features in reflection high-energy electron diffraction (RHEED) patterns. Gold nanoparticles (80-nm-diameter AuNPs in citrate buffer) from BBI Solutions were dropcast on the substrate to a number density of ~10^{-3} μm^{-2} on the STO surface. A 350-nm layer of parylene-C (SCS Labcoter 2) was deposited on top of the entire sample and then etched with O$_2$ plasma to expose the top of the AuNPs while leaving a 20-nm insulating layer around the particles. Etching was performed in steps while monitoring the parylene thickness with an ellipsometer (Woollam alpha-SE).

Sample characterization. The phase and crystalline quality of the thin films were investigated by ω–2θ X-ray diffraction (using a high-resolution Panalytical Empyrean vertical diffractometer, Cu Kα radiation) and high-resolution transmission electron microscopy (HRTEM, FEI FEI Talos 200X TEM). The surface morphologies were examined by AFM. HRTEM images, selected area

diffraction (SAD) patterns and EDX elemental maps (Supplementary Fig. 4) were used to estimate layer thicknesses and show the presence of the TiO_2 layer between the STO and TiN.

Optical set-up. The plasmon resonances of the AuNPs were characterized by scattering spectra and colour images. The sample was illuminated by high-angle white light incident through a ×100 DF 0.8-NA objective (LMPlanFLN) in an optical dark-field configuration. The same objective was used for collection of scattering spectra and images. The dark-field scattered light was sent to a CCD camera (Lumenera Infinity 2) and spectrometer (Ocean Optics QE65000) for spectral analysis. The spectral content of the scattered light was measured with 1-s or 0.5-s integration times (the time resolution is limited by the light intensity, with brighter light sources capable of bringing integration times down to 10 ms).

Electrical measurements. For electrical characterization, a Keithley 2635 source meter was used in a four-wire configuration with triaxial connections, which allows low-noise measurement of currents down to 10 pA. In all measurements, the Au top electrode was grounded. The voltage was ramped and a sweep rate of $0.18\,V\,s^{-1}$ was used. A measurement range of $100\,\mu A$ was used to keep the integration time and sweep rate constant. All measurements were performed in air at room temperature.

Cantilever contacting. Transparent tip-less SiN AFM cantilevers were coated with 3-nm Cr and 6-nm Au by electron-beam evaporation, providing a transparent conductive coating. Tips were mounted on a custom-built mount controlled by *XYZR* piezoelectric positioners and integrated with the microscopy set-up. The cantilever spring constant was $k = 35\,mN\,m^{-1}$ (as measured during manufacture), resulting in a pressure on our gap region of 0.04 GPa (Supplementary Section G).

Numerical simulations. DFT calculations were carried out using the plane wave pseudopotential code CASTEP[42]. The optical dielectric functions were calculated by OptaDOS[43]. A commercial simulator based on the FDTD method was used to perform calculations of the far-field scattering spectra and near-field distributions (Lumerical Inc., https://www.lumerical.com/products/).

Data availability

References

1. Siemon, A. et al. Realization of Boolean logic functionality using redox-based memristive devices. *Adv. Funct. Mater.* **25**, 6414–6423 (2015).
2. Valov, I., Waser, R., Jameson, J. R. & Kozicki, M. N. Electrochemical metallization memories—fundamentals, applications, prospects. *Nanotechnology* **22**, 289502 (2011).
3. Waser, R. & Aono, M. Nanoionics-based resistive switching memories. *Nat. Mater.* **6**, 833–840 (2007).
4. Bernard, Y., Renard, V. T., Gonon, P. & Jousseaume, V. Back-end-of-line compatible conductive bridging RAM based on Cu and SiO_2. *Microelectron. Eng.* **88**, 814–816 (2011).
5. Das, M., Kumar, A., Singh, R., Htay, M. T. & Mukherjee, S. Realization of synaptic learning and memory functions in Y_2O_3 based memristive device fabricated by dual ion beam sputtering. *Nanotechnology* **29**, 055203 (2018).
6. Niu, D., Chen, Y., Xu, C. & Xie, Y. Impact of process variations on emerging memristor. In *Proceedings of the 47th Design Automation Conference* 877–882 (Association for Computing Machinery, 2010); https://doi.org/10.1145/1837274.1837495
7. Kwon, D.-H. et al. Atomic structure of conducting nanofilaments in TiO_2 resistive switching memory. *Nat. Nanotechnol.* **5**, 148–153 (2010).
8. Chen, J.-Y. et al. Dynamic evolution of conducting nanofilament in resistive switching memories. *Nano Lett.* **13**, 3671–3677 (2013).
9. Choi, B. J. et al. Resistive switching mechanism of TiO_2 thin films grown by atomic-layer deposition. *J. Appl. Phys.* **98**, 033715 (2005).
10. Szot, K., Speier, W., Bihlmayer, G. & Waser, R. Switching the electrical resistance of individual dislocations in single-crystalline $SrTiO_3$. *Nat. Mater.* **5**, 312–320 (2006).
11. Yang, J. J. et al. The mechanism of electroforming of metal oxide memristive switches. *Nanotechnology* **20**, 215201 (2009).
12. Das, M. et al. Effect of surface variations on the performance of yttria based memristive system. *IEEE Electron Device Lett.* **39**, 1852–1855 (2018).
13. Ahmed, T. et al. Inducing tunable switching behavior in a single memristor. *Appl. Mater. Today* **11**, 280–290 (2018).
14. Sun, B. et al. The effect of current compliance on the resistive switching behaviors in $TiN/ZrO_2/Pt$ memory device. *Jpn J. Appl. Phys.* **48**, 04C061 (2009).
15. Krishnan, K., Aono, M. & Tsuruoka, T. Kinetic factors determining conducting filament formation in solid polymer electrolyte based planar devices. *Nanoscale* (2016); https://doi.org/10.1039/C6NR00569A
16. Menzel, S., Böttger, U., Wimmer, M. & Salinga, M. Physics of the switching kinetics in resistive memories. *Adv. Funct. Mater.* **25**, 6306–6325 (2015).
17. Tappertzhofen, S., Menzel, S., Valov, I. & Waser, R. Redox processes in silicon dioxide thin films using copper microelectrodes. *Appl. Phys. Lett.* **99**, 203103 (2011).
18. Hubbard, W. A. et al. Nanofilament formation and regeneration during Cu/Al_2O_3 resistive memory switching. *Nano Lett.* **15**, 3983–3987 (2015).
19. D'Aquila, K., Liu, Y., Iddir, H. & Petford-Long, A. K. In-situ TEM study of reversible and irreversible electroforming in Pt/Ti:NiO/Pt heterostructures. *Phys. Status Solidi Rapid Res. Lett.* **9**, 301–306 (2015).
20. Yang, Y. & Lu, W. D. Progress in the characterizations and understanding of conducting filaments in resistive switching devices. *IEEE Trans. Nanotechnol.* **15**, 465–472 (2016).
21. Di Martino, G., Tappertzhofen, S., Hofmann, S. & Baumberg, J. Nanoscale plasmon-enhanced spectroscopy in memristive switches. *Small* **12**, 1334–1341 (2016).
22. Emboras, A. et al. Atomic scale photodetection enabled by a memristive junction. *ACS Nano* **12**, 6706–6713 (2018).
23. Emboras, A. et al. Atomic scale plasmonic switch. *Nano Lett.* **16**, 709–714 (2016).
24. Waser, R. *Nanoelectronics and Information Technology: Advanced Electronic Materials and Novel Devices* (Wiley, 2012).
25. Valov, I. Interfacial interactions and their impact on redox-based resistive switching memories (ReRAMs). *Semicond. Sci. Technol.* **32**, 093006 (2017).
26. Cho, S. et al. Self-assembled oxide films with tailored nanoscale ionic and electronic channels for controlled resistive switching. *Nat. Commun.* **7**, 12373 (2016).
27. Baumberg, J. J., Aizpurua, J., Mikkelsen, M. H. & Smith, D. R. Extreme nanophotonics from ultrathin metallic gaps. *Nat. Mater.* **18**, 668–678 (2019).
28. Ranjan, A. et al. Analysis of quantum conductance, read disturb and switching statistics in HfO_2 RRAM using conductive AFM. *Microelectron. Reliab.* **64**, 172–178 (2016).
29. Aravind, P. K. & Metiu, H. The effects of the interaction between resonances in the electromagnetic response of a sphere-plane structure; applications to surface enhanced spectroscopy. *Surf. Sci.* **124**, 506–528 (1983).
30. Nordlander, P. & Prodan, E. Plasmon hybridization in nanoparticles near metallic surfaces. *Nano Lett.* **4**, 2209–2213 (2004).
31. Lian, X. et al. Multi-scale quantum point contact model for filamentary conduction in resistive random access memories devices. *J. Appl. Phys.* **115**, 244507 (2014).
32. Long, S. et al. Quantum-size effects in hafnium-oxide resistive switching. *Appl. Phys. Lett.* **102**, 183505 (2013).
33. Cartoixà, X., Rurali, R. & Suñé, J. Transport properties of oxygen vacancy filaments in metal/crystalline or amorphous HfO_2/metal structures. *Phys. Rev. B* **86**, 165445 (2012).
34. Mertens, J. et al. Tracking optical welding through groove modes in plasmonic nanocavities. *Nano Lett.* **16**, 5605–5611 (2016).
35. Mertens, J. et al. Controlling subnanometer gaps in plasmonic dimers using graphene. *Nano Lett.* **13**, 5033–5038 (2013).
36. Tserkezis, C. et al. Hybridization of plasmonic antenna and cavity modes: extreme optics of nanoparticle-on-mirror nanogaps. *Phys. Rev. A* **92**, 053811 (2015).
37. Demetriadou, A. et al. Spatiotemporal dynamics and control of strong coupling in plasmonic nanocavities. *ACS Photonics* **4**, 2410–2418 (2017).
38. Pflüger, J. & Fink, J. in *Handbook of Optical Constants of Solids* (ed. Palik, E. D.) Ch. 13, 293–311 (Academic Press, 1997); https://doi.org/10.1016/B978-012544415-6.50055-8
39. Pflüger, J., Fink, J., Weber, W., Bohnen, K. P. & Crecelius, G. Dielectric properties of TiC_x, TiN_x, VC_x and VN_x from 1.5 to 40 eV determined by electron-energy-loss spectroscopy. *Phys. Rev. B* **30**, 1155–1163 (1984).
40. Kos, D. et al. Electrically controlled nano and micro actuation in memristive switching devices with on-chip gas encapsulation. *Small* **14**, 1801599 (2018).
41. Li, Y. et al. Nanoscale chemical and valence evolution at the metal/oxide interface: a case study of Ti/$SrTiO_3$. *Adv. Mater. Interfaces* **3**, 1600201 (2016).
42. Clark, S. J. et al. First principles methods using CASTEP. *Z. Kristallogr.* (2005); https://doi.org/10.1524/zkri.220.5.567.65075
43. Morris, A. J., Nicholls, R. J., Pickard, C. J. & Yates, J. R. OptaDOS: a tool for obtaining density of states, core-level and optical spectra from electronic structure codes. *Comput. Phys. Commun.* **185**, 1477–1485 (2014).

Acknowledgements

Author contributions

Experiments were devised by G.D.M. and J.J.B. and performed by G.D.M., with support for the chemical nanoassembly and sample preparation from D.K. The custom-made cantilever contacting set-up was realized by D.K. W.L. synthesized the STO/TiN films, performed X-ray diffraction and atomic force microscopy, with support from X.W. and H.W. for the TEM measurements. DFT calculations were performed by B.Z., guided by W.L., and FDTD simulations by A.D. The data analysis was performed by G.D.M., with support from all authors. The manuscript was written with contributions from all authors.

Competing interests

The authors declare no competing interests.

Additional information

Supplementary information is available for this paper at https://doi.org/10.1038/s41928-020-00478-5.

Correspondence and requests for materials should be addressed to G.D. or J.J.B.

Reprints and permissions information is available at www.nature.com/reprints.

Publisher's note Springer Nature remains neutral with regard to jurisdictional claims in published maps and institutional affiliations.